Analyst

PAPER

View Article Online
View Journal

Cite this: DOI: 10.1039/d5an01181g

Diffusion kinetics of volatile organic compounds monitored by nanohole surface plasmonics

Swapnil Daxini,[a] Chris Prüfert,[b] Paul Reid,[a] Pedro Barros,[c] Juan Gomez-Cruz,[d] Carlos Escobedo,[e] Jack A. Barnes[f] and Hans-Peter Loock *[g]

Received 7th November 2025,
Accepted 23rd December 2025

DOI: 10.1039/d5an01181g

rsc.li/analyst

The extraordinary optical transmission, EOT, through a gold-film nanohole array was used to measure refractive index changes of a thin film of polydimethylsiloxane, PDMS, upon absorption of *o*-xylene gas. As *o*-xylene diffuses into the 10 μm thick PDMS film, the film swells slightly and its refractive index increases. The PDMS index change produces a red-shift of the EOT maximum which is observable in a simple optical transmission spectrum. Since the experiments are fast (<200 ms) and precise (<2 × 10^{-4} RIU) we can follow the kinetics of the diffusion process with enough accuracy to distinguish two distinct diffusion mechanisms that occur at different time scales.

Introduction

The detection of anthropogenic and biogenic volatile organic compounds (VOCs) is an important field in gas phase analysis and is relevant to, for example, food production, environmental monitoring, health care and industrial processes.[1–7] Benzene, toluene, ethylbenzene and xylenes (BTEX) form a subcategory of VOCs, whose monitoring is of particular importance as they pose a considerable risk to human health at high concentration and/or prolonged exposure. Health risks include but are not limited to respiratory diseases, reproductive adversities, and cancer.[8,9]

BTEX compounds are typically analysed using separation techniques such as gas chromatography-mass spectrometry (GC-MS), high-performance liquid chromatography (HPLC), and capillary electrophoresis (CE). Samples can be controllably enriched in BTEX concentrations using Solid-Phase Micro-Extraction (SPME), a rapid, solvent-free sample preparation method pioneered by the Pawliszyn group and others.[10,11] Polydimethylsiloxane (PDMS) is a commonly used extraction matrix for SPME, as it is an elastic, chemically inert hydrophobic polymer that strongly interacts with non-polar molecules and readily absorbs BTEX from both liquids and gas samples.[12] To optimize PDMS-SPME probes for optimum extraction time and film thickness, it is important to understand the diffusion kinetics of these compounds through PDMS.

The diffusion kinetics through polymers have previously been investigated through gravimetric sensors,[13,14] time-lag permeation,[15] and through the measurement of refractive index and swelling using a interferometric refractometer.[16,17] In this paper, we present a real-time, on-line, continuous, cost-effective VOC sensing method that is based on the phenomenon of extraordinary optical transmission (EOT) to investigate the diffusion kinetics of *o*-xylene into PDMS.

When light is incident on an array of sub-wavelength holes in a gold or silver film, one observes higher than expected transmission for a range of wavelengths. White light from a broad band light source is thereby filtered such that some colours are blocked, and others are transmitted though the holes to an extent that is higher than expected from classical aperture theory alone.[18]

The EOT resonance occurs due to the photonic excitation of surface plasmon polaritons (SPPs) on the metallic surface of the noble metal film. Like surface plasmon resonance (SPR) sensors, EOT-based sensors are sensitive to the changes of the refractive index (RI) at the interface between the metal film and the dielectric medium surrounding it.[18–21] They can be used to measure the refractive index of liquids[22] and polymers covering the array.[23] Contrary to other optical techniques that are used for VOC detection, nanohole array sensors can be interrogated in transmission mode, allowing for easier alignment, miniaturization and multiplexing.[24,25] A conventional absorption spectrometer suffices for the measurement of the EOT signal. The fabrication of the device presented in this work is facile, rapid, and does not require a cleanroom.

Following the publication of the seminal work on EOT by Ebbesen *et al.* in 1998,[18] there have been numerous sensing

[a]*Dept. of Physics, University of Victoria, Victoria, B.C., Canada V8N 5C2*
[b]*Inst. of Chemistry, Physical Chemistry, University of Potsdam, 14469 Potsdam, Germany*
[c]*Dept. of Biochemistry, University of Victoria, Victoria, B.C., Canada V8N 5C2*
[d]*Spectra Plasmonics, Kingston, ON, Canada K7L 0E9*
[e]*Dept. of Chemical Engineering, Queen's University, Kingston, ON, Canada K7L 3N6*
[f]*Dept. of Chemistry, Queen's University, Kingston, ON, Canada K7L 3N6*
[g]*Dept. of Chemistry, University of Victoria, Victoria, B.C., Canada V8N 5C2. E-mail: hploock@uvic.ca*

systems based on nanohole arrays for refractometry,[20,22,26] biosensing,[20,27,28] as well as in multiplexed systems.[28,29] Recent work has demonstrated the use of nanohole arrays for gas detection,[30,31] though the systems were based on monitoring intensity changes, rather than the plasmonic shift induced by refractive index changes, and may therefore be more prone to noise from the light source and detector. The design parameters guiding the optimization of EOT-based sensors were recently reviewed by Asif and Sahin.[32]

In the present study, we demonstrate the use of a PDMS-covered EOT system as a novel VOC sensing method. With the high time-resolution and high sensitivity that this sensor affords, we obtain insights into the diffusion kinetics of *o*-xylene into PDMS. The kinetics of *o*-xylene diffusion through a thin layer of PDMS are investigated by measuring the peak-shift of the plasmonic signal. To the best of our knowledge, this study is the first application of EOT spectroscopy to the measurement of gaseous analytes, representing, also, the first integration of solid-phase microextraction of gases with EOT-based plasmonic sensing.

In contrast to conventional plasmonic devices, and many previously reported EOT-based sensors, the present configuration eliminates the need for micro- or nanofabrication. The nanohole array is instead obtained by sputter-coating a commercial Transmission Electron Microscopy (TEM) support grid with a thin gold film, providing a facile and reproducible platform for optical measurements. The refractive index is obtained from an optical transmission spectrum that is recorded using a simple optical setup. The system also incorporates a compact and intuitively designed nebulizer that offers high accuracy and adjustability over a wide range of partial pressures. The diffusion model described in the SI is derived from a new and rigorous integration of Fick's one-dimensional diffusion law. A comprehensive discussion of this theoretical framework is forthcoming.

Experimental setup

The PDMS-coated nanohole array (NHA), was mounted into a 3D-printed chamber, and was interrogated in a transmission configuration with collimated light from a broadband light source (LS-1 Tungsten halogen lamp, Ocean Optics, USA). The EOT output spectrum was collected with a fiber-coupled UV-Vis spectrometer (USB4000, Ocean Optics, USA) (Fig. 1).

The 3D-printed chamber allows for the introduction of gas either above the PDMS layer or from the underside of the NHA. A nebulizer system was developed to generate different VOC loads in the carrier gas in a compact, resource-efficient way, allowing for adjustable and small loadings (<4000 ppm) of VOC in nitrogen gas. The dual gas-stream system can supply the chamber with only carrier gas (N_2) or with analyte-containing gas from the output of the nebulizer system.

The nebulizer consists of two co-axially mounted capillaries, with the inner capillary supplying the liquid VOC through a syringe pump. Due to the steep pressure gradient,

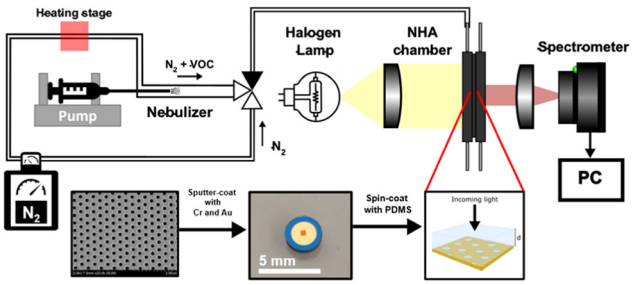

Fig. 1 Schematic overview of the setup with the NHA preparation, nebulization stage and optical setup.

strong sheer forces are exerted on the liquid at the tip of capillary. This leads to the dispersion of the ejected liquid into a fine mist, *i.e.* the liquid is nebulized. The flow of heated nitrogen gas from the surrounding larger capillary carries the mist towards the sample chamber while ensuring complete evaporation of the VOC. Since the liquid and gas flow rates can be tightly controlled, the VOC partial pressure of the sample gas can be finely adjusted with about 10 ppm accuracy in the range of 10 ppm to 4000 ppm. A Computational Fluid Dynamics, CFD, simulation of the nebulizer is provided in the SI.

Nanohole array fabrication and assembly

The plasmonic NHA sensor head was prepared from a commercial sample-mounting grid designed for transmission electron microscopy, TEM, that we coated with gold. The hexagonal Si_3N_4 nanohole grid (Ted Pella Inc., USA) was plasma-cleaned for 60 s and sputter coated, first, with 5 nm of Cr as an adhesion layer and then, with 100 nm of gold. A scanning electron micrograph, SEM, is provided in the SI (see also Fig. 1).

The depth range of the refractive index measurements is governed by the penetration depth of the surface plasmons; thus, it is essential to have strong adhesion between the PDMS and gold layer. As gold bonds only weakly to PDMS, we used (3-mercaptopropyl) trimethoxysilane (MPTMS) (Sigma-Aldrich, USA) as a molecular adhesive.[33] The gold-coated NHAs were plasma-cleaned and submersed in a 10 mM ethanolic solution of MPTMS for 20 hours to produce an MPTMS monolayer. The MPTMS was then activated *via* plasma cleaning for 60 s before a PDMS (Dow Corning Sylgard 184, 10 : 1 mixing ratio) layer was spin-coated onto the NHA directly thereafter. The NHA was mounted onto the spin-coater, the PDMS was drop-cast onto the NHA, and spin-coated with the desired thickness – here 10 μm. The spin-coating procedure was facilitated by mounting the NHA onto a 3D-printed mount. This 3D-printed component was affixed onto the spin coater with adhesive tape. The thickness was set according to a calibration curve obtained using an optical profiler (see SI). After spin-coating, the PDMS film was cured for 10 min at 100 °C and 20 min at 70 °C on a hotplate. Since the diffusion rate of VOCs through PDMS depends strongly on the crosslinking density of the polymer film, care was taken to maintain a similar PDMS

mixing ratio and preparation procedure to reproduce the cross-linking density, accurately.

The chamber holding the PDMS-coated NHA was designed in-house and resin-printed using a 3D printer. It consists of three main parts, *i.e.* two outer plates and one central disc with a slot that holds the NHA. The chamber was designed so that the gas exchange rate in the chamber (≈15 ms) is much smaller than the diffusion time constant (τ > 10 s), such that the PDMS diffusion governs the measurements' response time. The plates have a 5 mm × 5 mm square open hole that is turned into an optical window using microscopy coverslip squares (Fisher Scientific, USA) that are attached and sealed using epoxy resin. On its inside face, each plate has a square center recess that forms the sample chamber. The sample chamber accepts sample gas through a bore connected with 22 needle gauge tubing to the aerosol generator, while the second bore directs the sample gas to waste after it has flown across the PDMS film which faces the white light source. The right part of the chamber (Fig. 1) has a similar design and, therefore, also permits gas flow across the silicon nitride grid that forms the support for the NHA assembly.

In the present study, all the results were obtained with the sample gas flowing through the PDMS layer towards the gold-coated NHA substrate layer as this gives better insight on the diffusion kinetics through the PDMS layer.

When reversing the gas flow from the NHA substrate towards the unsupported PDMS film surface, we observed a much faster sensor response as the analyte interacts with the plasmonic field immediately. Unfortunately, the measurements were difficult to reproduce, likely because of partial delamination of the PDMS layer due to pressure from the gas flow.

Data pre-processing

The centroid wavelength of the EOT peak was used as a measure of the wavelength of the EOT resonance instead of the maximum of the peak. The centroid corresponds to the "centre of mass" of the peak and was calculated using the top 50% of the EOT transmission peak. Using the centroid wavelength is advantageous, if the EOT contribution of interest (here arising from plasmonic interactions at the PDMS–Au interface) spectrally overlaps with other EOT contributions such as those from the substrate–Au interface. Prior to determining the peak centroid, the Savitzky–Golay filter was used on the spectrum to reduce the noise, resulting in fewer outliers in the centroid calculation.

We averaged ten consecutive EOT spectra, and the average centroid wavelength is calculated with its respective standard error and with acquisition times ranging from 200 ms to 2s.

Theoretical models

Mole fraction calculations

After calibration of the sensor one can determine the refractive index of the PDMS from the experimentally observed using centroid wavelength of the EOT spectrum. Next, the average mole fraction, $\bar{X}(t)$, of the analyte that is absorbed in the section of the film interrogated by the surface plasmon polaritons can be calculated from the film's refractive index, n_{mix}, using (1), an equation that had been derived previously,[16]

$$\bar{X}(t) = \frac{P_{\mathrm{PDMS}}\left[1 - \left(\frac{{n_{\mathrm{PDMS}}}^2 + 2}{{n_{\mathrm{PDMS}}}^2 - 1}\right)\left(\frac{{n_{\mathrm{mix}}}^2(t) - 1}{{n_{\mathrm{mix}}}^2(t) + 2}\right)\right]}{P_{\mathrm{PDMS}}\left[1 - \left(\frac{{n_{\mathrm{PDMS}}}^2 + 2}{{n_{\mathrm{PDMS}}}^2 - 1}\right)\left(\frac{{n_{\mathrm{mix}}}^2(t) - 1}{{n_{\mathrm{mix}}}^2(t) + 2}\right)\left(1 + \frac{\Delta d(t)}{d_0}\right)\right] - P_{\mathrm{analyte}}} \quad (1)$$

In deriving (1), it is assumed that the Lorenz–Lorentz equation holds, *i.e.* that molar polarizabilities, P_i, are linearly additive. Note that refractive indices, n_i, are not linearly additive. In this case, we also assume that swelling of the film is negligible (Δd = 0). Although it has been observed that PDMS swells by up to 50% after 72 hours of exposure to a saturated xylene atmosphere,[34] the assumption holds in our experiments, since the sorption experiments were much shorter and at a lower xylene concentration. Indeed, the maximum swelling was measured to be between 2–5% and assumed negligible for the modelling. The maximum swelling upon absorption was determined from a weak thin film interference spectrum observed in many of the EOT spectra (see SI).

Diffusion constants of the VOCs

Since the experiments are conducted at temperatures well above the PDMS glass transition temperature, T_g = −123 °C,[35] the analyte migration into a polymer can be modelled by a one-dimensional Fickian diffusion mechanism[36]

$$\frac{\mathrm{d}X}{\mathrm{d}t} = D\frac{\partial^2 X}{\partial y^2}. \quad (2)$$

The PDMS layer on the surface is thin compared to its lateral extension, and the hole diameter is orders of magnitude smaller than the film thickness. Therefore, the problem was analysed as one-dimensional diffusion through a sheet of finite thickness having an infinite reservoir of analyte gas above the polymeric sorption film. Most of this PDMS film is supported by the gold film which is assumed to be an impenetrable substrate (described as a "supported film"), whereas a smaller fraction is suspended above the nanoholes ("free-standing film").

We now introduce, briefly, the kinetic model of the absorption and desorption of an analyte into a thin film supported by an array of nanoholes. In our derivation we integrate Crank's solutions for a one-dimensional diffusion problem.[37] When neglecting lateral diffusion, the problem can be understood as a linear combination of Crank's solution for a film mounted on an impermeable support and the solution for a free-standing film.

Eqn (4) and (6) for a supported film have been presented, previously.[16] Their derivations by integration of the Crank's equations, as well as the derivation of the new eqn (3) and (5) for a free-standing film, are given in the SI. The average mole fraction of the analyte over the film sliver sampled by the eva-

nescent wave near metal-film interface is given by $\bar{X}_{SF}$ for a supported film (SF), and by $\bar{X}_{FSF}$ for a free-standing film (FSF). The sliver's thickness is determined by a Finite-Difference Time-Domain, FDTD, simulation, see Fig. 2. The weighted linear combination of these contributions is determined separately for absorption processes (abs) in eqn (3) and (4) and desorption processes (des) in eqn (5) and (6). In these equations X_∞ is the equilibrium mole fraction in the film, and the diffusion coefficient D is calculated from the fit to (7).

The film thickness, d = 10.2 μm was obtained using an optical profiler (see SI), and δy is the effective amplitude of the evanescent plasmonic wave into the PDMS and is obtained by modelling – see below and Fig. 2. The weighing coefficients can be estimated using the cross-sectional areas of holes (FSF) and the gold film (SF). The total sensing area is 2.0×10^5 μm^2, and the nanoholes, representing the FSM, account for 4.0×10^4 μm^2 or 20% of the total area. Therefore, the linear combination representing the total solvent mole fraction can be estimated as:

$$\begin{aligned}\bar{X}_{abs} &= 0.8\bar{X}_{abs,SF} + 0.2\bar{X}_{abs,FSF}\\ \bar{X}_{des} &= 0.8\bar{X}_{des,SF} + 0.2\bar{X}_{des,FSF}\end{aligned} \quad (3)$$

A more rigorous determination of this 4 : 1 ratio, accounting for the overlap of the evanescent wave with the PDMS film, is given below and in the SI.

As will be discussed below, most processes are best analysed as concurrent sorption processes having *two* different diffusion rates given by D_1 and D_2, and (3) is therefore best written as

$$\begin{aligned}\bar{X}_{abs} &= 0.8\left[a_1\bar{X}_{abs,SF}(D_1) + a_2\bar{X}_{abs,SF}(D_2)\right]\\ &\quad + 0.2\left[a_1\bar{X}_{abs,FSF}(D_1) + a_2\bar{X}_{abs,FSF}(D_2)\right]\\ \bar{X}_{des} &= 0.8\left[b_1\bar{X}_{des,SF}(D_1) + b_2\bar{X}_{des,SF}(D_2)\right]\\ &\quad + 0.2\left[b_1\bar{X}_{des,FSF}(D_1) + b_2\bar{X}_{des,FSF}(D_2)\right]\end{aligned} \quad (4)$$

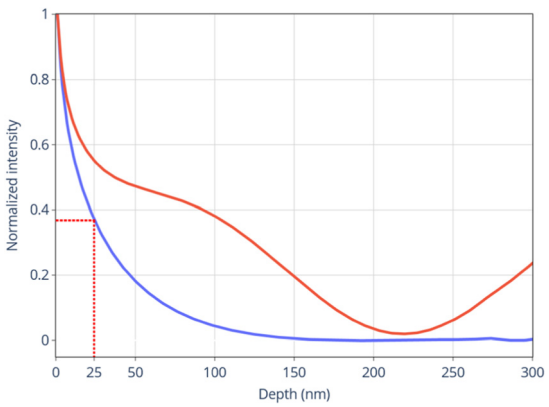

Fig. 2 Calculation of the depth of the evanescent wave into the PDMS layer. The red curve shows the total average electric field intensity as a function of distance from the NHA support, which includes the contribution from the reflected field. After subtracting the sinusoidal contribution from the reflected radiation, the exponential curve (blue) shows an evanescent intensity decay length of 25 nm, *i.e.* the length at which the intensity decays by 1/e.

where a_1, a_2, b_1, b_2, D_1 and D_2 are the parameters that are optimized in a least-squares fitting algorithm.

$$\bar{X}_j(t)_{abs,FSF} = a_j\left[\frac{\delta y}{2d} + \frac{2d}{\pi^2\delta y}\sum_{i=1}^{\infty}\frac{(-1)^i}{i^2}\exp\left(-\frac{D_j(t-t_0)i^2\pi^2}{d^2}\right)\left(1-\cos\frac{i\pi\delta y}{d}\right)\right];\quad j = 1,2 \quad (5)$$

$$\bar{X}_j(t)_{abs,SF} = a_j\left[1 - \frac{8d}{\pi^2\delta y}\sum_{i=0}^{\infty}\frac{(-1)^i}{(2i+1)^2}\exp\left(-\frac{D_j(t-t_0)(2i+1)^2\pi^2}{4d^2}\right)\times\sin\left(\frac{(2i+1)\pi\delta y}{2d}\right)\right] \quad (6)$$

$$\bar{X}_j(t)_{des,FSF} = b_j\left[\frac{4d}{\delta y\pi^2}\sum_{i=0}^{\infty}\frac{1}{(2i+1)^2}\exp\left(-\frac{D_j(t-t_0)(2i+1)^2\pi^2}{d^2}\right)\left(1-\cos\frac{(2i+1)\pi\delta y}{d}\right)\right];\quad j = 1,2 \quad (7)$$

$$\bar{X}_j(t)_{des,SF} = b_j\left[\frac{8d}{\pi^2\delta y}\sum_{i=0}^{\infty}\frac{(-1)^i}{(2i+1)^2}\exp\left(-\frac{D_j(t-t_0)(2i+1)^2\pi^2}{4d^2}\right)\times\sin\left(\frac{(2i+1)\pi\delta y}{2d}\right)\right] \quad (8)$$

EOT simulation

To investigate the spatial extent, δy, of surface plasmon resonance (SPR) interactions within the system we conducted a three-dimensional FDTD simulation (Tidy3D 2.8.4, Flexcompute). Periodic boundary conditions were applied along the x and y directions (1.4 μm and 1.2 μm, respectively), corresponding to a small section of the hexagonal NHA. Along the z-axis, perfectly matched layers, PMLs, were implemented to absorb outgoing waves and reduce reflections. To ensure the highest resolution near the plane of interaction an override mesh (size: 7 nm in x- and y-direction and 0.5 nm in z-direction) was employed throughout the segment and with a height of 600 nm, centred about the TEM grid. The PDMS film, the Cr adhesion layer, and the silicon nitride substrate were modelled using the Sellmeier dispersion relation with parameters obtained from the Tidy3D database,[38–40] while the optical response of gold was described using a Drude model, as it more accurately captures its plasmonic behaviour.[41]

The FDTD simulation was used to determine the electric field's spatial distribution across the gold surface and at various depths within the PDMS. This was used to estimate the ratio of the sensing areas between the supported film and the free-standing film in (3). Details in the SI show that the ratio is nearly identical to the 4 : 1 ratio estimated from the fractional areas in the previous section.

In addition, the integrated field intensity at the SPR resonance wavelengths was used to evaluate the decay lengths of

the SPR-induced fields into the PDMS material to estimate δy = 25 nm, as the effective decay length of the evanescent plasmonic wave (Fig. 2). In this figure, the normalized average electric field intensity is calculated in 0.5 nm steps into the PDMS layer. The sinusoidal reflected field was subtracted from the average intensity to retrieve the evanescent field from the plasmonic interaction at the interface. This decay length, δy, governs the thickness of the layer in which the refractive index change can be measured, *i.e.* it corresponds to the bounds of the integrals that lead to eqn (3)–(6) (SI).

The wavelengths of the EOT resonances for a periodic hexagonal lattice array of nanoholes can also be approximated using momentum conservation matching conditions,[42] given by

$$\lambda_{\max_{i,j}} = \frac{\Lambda}{\sqrt{\frac{4}{3}(i^2 + ij + j^2)}} \sqrt{\frac{\varepsilon_m \varepsilon_d}{\varepsilon_m + \varepsilon_d}} \quad (9)$$

where Λ is the period of array, i and j are resonance orders, ε_m and ε_d are the dielectric constants of the metal and dielectric, respectively. Fig. 3 shows experimental EOT spectra for two different refractive indices. The location of approximate resonances due to the PDMS–Au interface and Au–Si_3N_4 interface are predicted by eqn (9) and plotted as gold and gray arrows respectively.

Calibration curve and sensitivity

The diffusion mechanism of *o*-xylene through PDMS can be determined by measuring the time-dependent mole fractions of *o*-xylene in the PDMS layer adjacent to the gold-film. The mole fractions are obtained from the refractive indices during that process. Over the small refractive index range that we study, the experimentally obtained wavelength shift of the EOT maximum (obtained using the centroid of the top 50% of the peak) correlates linearly with the change in the refractive index of the dielectric medium above the gold layer. A calibration series of mixtures of glycerol ($C_3H_8O_3$, n = 1.475) and water (n = 1.333 at 589 nm[43]) was used to obtain the sensor's sensitivity as S = 170 ± 3 nm per refractrive index unit (RIU) (Fig. 4). The refractive indices of the water–glycerol mixtures were determined using a handheld digital refractometer (Item #81150-56, Cole-Parmer). The confidence intervals and the residuals indicate that the refractive index in this range can be obtained with an average 1σ uncertainty of Δn = 0.002 RIU, which is limited by the accuracy of the reference refractometer.

To perform the calibration, the NHA was placed in a PDMS mould having a 50 μm open channel to allow for the flow of calibration solutions using a peristaltic pump. Each solution was directed over the NHA for a minimum of 60 s and the average centroid wavelength for each mixture was obtained.

Results

Fig. 5 shows the mole fraction of *o*-xylene in the boundary layer to the gold surface, measured through the observed shift of the centroid wavelength, as a function of time and at different *o*-xylene partial pressures (30 Pa = 295 ppm = 1 μL min^{-1}). By inspection, it is apparent that with increasing gas concentrations the rate of uptake of *o*-xylene into the film increases, and that the desorption rate also increases. In addition, the equilibrium value that is reached for each of the *o*-xylene partial pressures increases with increasing concentration, consistent with SPME principles.[11] It is also apparent that gas concentrations above 1770 ppm (179 Pa; 6 μL min^{-1}) show evidence for a second uptake process that occurs at a slower rate and leads to a much higher loading of the film. Especially the desorption curves show that the second slower process is time-delayed, as there is a clear step in the desorption curves.

In order to quantify the diffusion constants of the diffusion of *o*-xylene into PDMS, the absorption and desorption curves

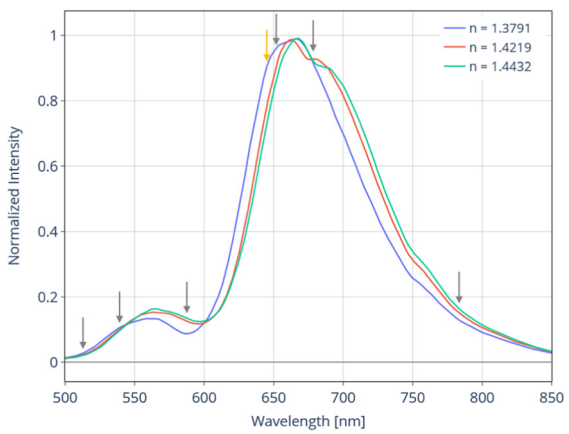

Fig. 3 EOT resonance spectrum for solutions with different refractive indices flowing over the NHA. The arrows represent the wavelength of the resonances due to plasmonic interaction as predicted by eqn (9) for the Au–Si_3N_4 (gray) and dielectric–Au (gold) interfaces. As the refractive index of the solution above the Au changes, we observe a changing peak shape as the contribution of the dielectric–Au EOT resonance shifts.

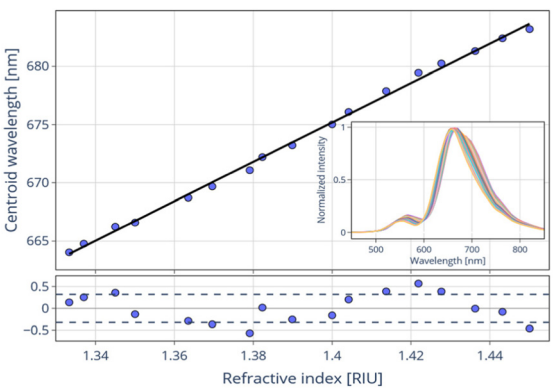

Fig. 4 Calibration of the sensor using mixtures of glycerol and water. The spectra of all solutions are shown in the inset. The linear fit yields the sensitivity of the RI measurement as S = 170 ± 3 nm per RIU. The width of the 1σ-confidence interval (0.8 nm) indicates that refractive index can be measured with an uncertainty of Δn = 0.002 RIU.

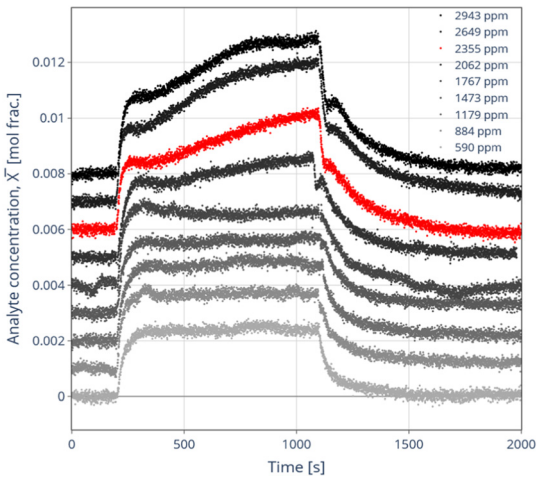

Fig. 5 Absorption and desorption curves for a nitrogen gas flow of 750 mL min^{-1} loaded with different concentrations of *o*-xylene sent through the nebulizer (with an added offset for visualization). For the first 200 s, pure N_2 is flown over the chamber to establish a baseline, followed by 900 s of *o*-xylene/N_2 flow and pure N_2 flow again for absorption and desorption respectively. The data highlighted in red are also shown in Fig. 6.

were fitted separately to (3)–(6). The curves were fit (LMfit python package[44]) with two diffusion coefficients *i.e.* using a weighted sum of the respective curves (3)–(6) as expressed in (4). Fig. 6 shows an example of the least-squares fit of the absorption and desorption using 2360 ppm *o*-xylene (238 Pa, 8 μL min^{-1} flow rate) to eqn (4) having two different rates. Here, the fast and slow sorption processes were assumed to start at the same time and to occur concurrently. We note that the step in Fig. 6, and, indeed, in all sorption curves with concentrations higher than 1770 ppm indicates that concurrent absorption may *not* be a good model. Introducing the time delay of the slower process as an additional fitting constant gave diffusion rates that were similar but had a larger uncertainty, since the additional fitting parameter made the model less constrained. For these practical reasons we retained the

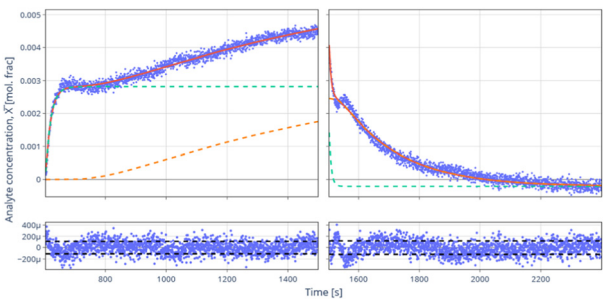

Fig. 6 Fitting of sorption curves with diffusion eqn (8). The fit (solid red line) is a linear combination of the bi-exponential fit (dashed green and orange line) for the absorption (D_1 = 3.0 × 10^{-8} cm^2 s^{-1}, D_2 = 9.0 × 10^{-10} cm^2 s^{-1}) and desorption (D_1 = 3.5 × 10^{-8} cm^2 s^{-1}, D_2 = 1.9 × 10^{-10} cm^2 s^{-1}). The residuals are displayed below each graph.

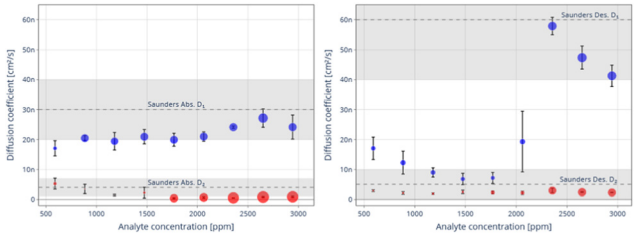

Fig. 7 Average absorption (left) and desorption (right) diffusion coefficients (D_1 and D_2 given in cm^2 s^{-1}) with the dashed grey line and shaded region representing previously obtained diffusion coefficients[16] for *m*-xylene with their uncertainties. The desorption D_1 diffusion coefficient for 2062 ppm (7 μL min^{-1}) shows a large uncertainty as not all fits were successful in capturing the second desorption process. A data table is provided in the SI.

assumption that the slow and fast processes start at the same time in our analysis.

An analysis similar to that shown in Fig. 6 was conducted for all concentrations of *o*-xylene and the two average diffusion coefficients for each flow rate were obtained by fitting. Each datum in Fig. 7 represents the average fitted diffusion coefficients, D_1, D_2, of at least three runs, with the uncertainty derived from standard error. The size of the circular data markers is proportional to the asymptotic concentration, a_1, a_2, b_1, b_2, of the respective equation in (4).

The diffusion constants for the absorption processes are averaged to $D_1 = (22 \pm 6) \times 10^{-9}$ cm^2 s^{-1} and $D_2 = (0.9 \pm 1.5) \times 10^{-9}$ cm^2 s^{-1}, whereas averaging the diffusion constants for the desorption processes yields $D_1 = (29 \pm 21) \times 10^{-9}$ cm^2 s^{-1} and $D_2 = (2.5 \pm 0.7) \times 10^{-9}$ cm^2 s^{-1} (see SI for the data table Fig. 7). These values are in fair agreement with those given by Saunders *et al.*[16] for the absorption of *m*-xylene into PDMS $D_1 = (30 \pm 10) \times 10^{-9}$ cm^2 s^{-1} and $D_2 = (4 \pm 3) \times 10^{-9}$ cm^2 s^{-1} and for the respective desorption processes $D_1 = (60 \pm 20) \times 10^{-9}$ cm^2 s^{-1} and $D_2 = (5 \pm 5) \times 10^{-9}$ cm^2 s^{-1}.

Discussion

The residuals in Fig. 6 may be used to estimate the uncertainty of the measurement. We can express this uncertainty either as the mole fraction of *o*-xylene in the film, $\delta X = \pm 0.0001$, or as the precision of the refractive index measurement $\delta n_{mix} = \pm 0.0001$ (see eqn (1)). The precision of the refractive index measurement is much better than the accuracy, $\pm \Delta n = 0.002$, obtained through the calibration curve in Fig. 4, which also depends on the accuracy of the RI values determined for the calibration solutions.

Fig. 7 shows that even at low concentrations of *o*-xylene the absorption and desorption curves can be well-fit using a process having two distinct diffusion constants. A data table is given in the SI. Both diffusion constants are consistent with earlier measurements of diffusion of *m*-xylene (not *o*-xylene) into a 20 μm-thick PDMS film interrogated by glancing angle thin-film interferometry.[16] The 1σ uncertainties of these pre-

viously obtained diffusion constants are given as grey bands in Fig. 7.

The more robust measurements at concentrations >1770 ppm (6 μL min^{-1}) give diffusion constants that fall into the lower range of previously obtained values. The difference may be due to the different diffusion rates of *m*-xylene used previously and *o*-xylene used here, the slightly different composition and crosslinking densities inherent with commercial PDMS formulations, or due to different boundary layer chemistry – our PDMS film is chemically bonded to a gold film, whereas in the previous measurement PDMS was spin-cast onto glass,[16] a plexiglass plate[45] or a rubber membrane.[46]

Importantly, the observed diffusion kinetics provide further evidence for a two-stage diffusion process as first reported by Saunders *et al.*[16] In their model, the VOC fills the pores within the PDMS resulting in a rapid change in refractive index. This process is followed by a slower absorption that changes the internal structure of the PDMS and causes it to swell. Both processes become faster with increasing VOC concentration of the surrounding gas, *i.e.* they are consistent with a first-order process.

The diffusion coefficients we obtained are consistent with measurements by Saunders *et al.* but they were 10-fold lower than those reported by other methods[13,45–47] for *o*-xylene and its isomers. This discrepancy has been rationalized by Saunders *et al.* as being due to (1) the difference in PDMS manufacturers which has been shown to result in different degrees of crosslinking, thereby altering the diffusion kinetics through the polymer, and (2) the inconsistency of the mathematical modelling of the diffusion process through the PDMS, which can change the diffusion constant by a factor of 2 for different models as reported by Lue *et al.*[13]

The second point is worth emphasizing: to the best of our knowledge, eqn (4) and (6) describing the diffusion through a supported film and our new eqn (3) and (5) for a free-standing film have not been used widely before. They arise from exact integration of Crank's equations[37] and are derived from the one-dimensional diffusion case described by Fick's second law (2). The more commonly used kinetic laws are usually written for the absorption process as

$$\bar{X}'(t)_{\mathrm{abs}} = X'_{\infty}\left[1 - \exp\left(-\frac{D'(t-t_0)}{d^2}\right)\right] \tag{10}$$

and for the desorption as

$$\bar{X}'(t)_{\mathrm{des}} = X'_{\infty}\exp\left(-\frac{D'(t-t_0)}{d^2}\right) \tag{11}$$

with little regard on whether the film is supported or not. Eqn (10) and (11) are first-order approximations to exact diffusion eqn (3)–(6), and yield diffusion constants that may be quite different compared to the exact equations.

In a forthcoming publication we will discuss the diffusion models for a supported film and for a free-standing film in more detail.

Conclusion

A simple and comparably inexpensive device exploiting the extraordinary optical transmission through a gold-covered nanohole array was used to record refractive index changes with an accuracy of 0.002 RUI. This accuracy is likely limited by our ability to determine the refractive index of the calibration solutions. The precision of the measurement (0.0001 RIU) is much higher and can be obtained from the wavelength change associated with the uptake of a high index VOC gas into a PDMS film that was applied as an SPME layer to the surface of the gold-NHA. The precision is ultimately limited by intensity noise in the spectrum which affects to a small extent the precision of the centroid wavelength determination. The temporal resolution of 200 ms per measurement is limited by the combination of the spectral acquisition rate and the time it takes to determine the centroid wavelength, which is the only parameter we retain from the measurements.

These uptake and desorption measurements allowed us to determine accurate diffusion constants using equations that were obtained by an integration of Crank's equations, which in turn are exact representations of Fick's second diffusion law. The measurements are consistent with previously reported values that were obtained on a similar chemical system but with a different device. The accuracy of the diffusion constants, D, is limited by the accuracy with which we know the film thickness, d, since any fit can only obtain the rise time as a ratio of d^2 and D, as apparent in the diffusion time constant

$$\tau = \frac{4d^2}{D\pi^2} \tag{12}$$

Consider that for $d = (10 \pm 2)$ μm and an assumed $D = 10 \times 10^{-9}$ cm^2 s^{-1}, the uncertainty in the reported absolute diffusion constant would be 40%.

Finally, we submit that the presented device can be seen as a single receptor in an "electronic nose", which may be combined with other receptors using different polymer extraction matrices to obtain an estimate of the chemical composition of a gas sample.

Author contributions

SD has contributed to conceptualization, investigation, data collection and analysis, visualization and to all stages of the writing process. CP has contributed to conceptualization, investigation, data curation, writing, review, and editing. PR performed many of the optical simulations. PB performed many of the adsorption and desorption measurements. JGC helped set up the experiments and advised on the chemical model. JAB derived the diffusion model equations. CE and HPL contributed to conceptualization, funding acquisition, project administration, supervision, writing, and editing.

Conflicts of interest

The authors declare no competing interests.

Data availability

The data sets used to generate the diffusion constants are available on Borealis, the Canadian Dataverse Repository, a bilingual, multi-disciplinary, secure, Canadian research data repository, supported by academic libraries and research institutions across Canada. Borealis supports discovery, management, sharing, and preservation of Canadian research data. The data and the code (functions described in eqn (3)–(6)) can be obtained from Daxini, Swapnil, 2026, "Replication Data for: Diffusion kinetics of volatile organic compounds monitored by nanohole surface plasmonics", https://doi.org/10.5683/SP3/EAVGPF, Borealis, V1, UNF:6:FzR6bIogj0hvt4lpoQEuTg== [fileUNF].

Supplementary information (SI) is available. The Supplementary Information contains details on the nebulizer design, the properties of the gold-film nanohole array (obtained by scanning electron microscopy), and the PDMS film thickness and its swelling upon o-xylene uptake. We also derive two models for the uptake and desorption of analytes into a supported film and free-standing film, respectively. Finally, we provide a FDTD calculation determining the fraction of the SPPs that interact with the PDMS near the holes and near the substrate, respectively. See DOI: https://doi.org/10.1039/d5an01181g.

Acknowledgements

This research was financially supported by the Natural Sciences and Engineering Research Council of Canada through the Discovery Grants program awarded to CE and HPL. The authors also acknowledge financial contributions by the University of Victoria and Queen's University.

References

1 P. Ciccioli, C. Silibello, S. Finardi, N. Pepe, P. Ciccioli, F. Rapparini, L. Neri, S. Fares, F. Brilli, M. Mircea, E. Magliulo and R. Baraldi, *Agric. For. Meteorol.*, 2023, **328**(19), 109255.
2 R. Epping and M. Koch, *Molecules*, 2023, **28**(19), 1598.
3 C. Di Fiore, P. Pandolfi, F. Carriera, A. Iannone, G. Settimo, V. Mattei and P. Avino, *Appl. Sci.*, 2023, **13**(11), 7344.
4 X. Bai, W. Liu, B. Wu, S. Liu, X. Liu, Y. Hao, W. Liang, S. Lin, L. Luo, S. Zhao, C. Zhu, J. Hao and H. Tian, *Environ. Pollut.*, 2023, **316**, 120600.
5 M. Fan, T. F. Rakotondrabe, G. Chen and M. Guo, *Food Chem.*, 2023, **418**, 135950.
6 A. Erler, D. Riebe, T. Beitz, H. G. Löhmannsröben, D. Grothusheitkamp, T. Kunz and F. J. Methner, *J. Mass Spectrom.*, 2020, **55**(10), e4501.
7 Q. Pan, Q.-Y. Liu, J. Zheng, Y.-H. Li, S. Xiang, X.-J. Sun and X.-S. He, *Environ. Int.*, 2023, **174**, 107886.
8 R. Montero-Montoya, R. López-Vargas and O. Arellano-Aguilar, *Ann. Glob. Health*, 2018, **84**, 225–238.
9 M. Masekameni, R. Moolla, M. Gulumian and D. Brouwer, *Int. J. Environ. Res. Public Health*, 2018, **16**, 95.
10 C. L. Arthur and J. Pawliszyn, *Anal. Chem.*, 1990, **62**, 2145–2148.
11 J. Pawliszyn, *Applications of solid phase microextraction*, Royal Society of Chemistry, Cambridge, 1st edn, 1999.
12 S. Seethapathy and T. Górecki, *Anal. Chim. Acta*, 2012, **750**, 48–62.
13 S. J. Lue, S. F. Wang, L. D. Wang, W. W. Chen, K.-M. Du and S. Y. Wu, *Desalination*, 2008, **233**, 277–285.
14 G. Dakroub, T. Duguet, C. Lacaze-Dufaure, S. Roualdes, A. van der Lee, D. Rebiscoul and V. Rouessac, *Plasma*, 2023, **6**, 563–576.
15 S. Sato, M. Suzuki, S. Kanehashi and K. Nagai, *J. Membr. Sci.*, 2010, **360**, 352–362.
16 J. E. Saunders, H. Chen, C. Brauer, M. Clayton and H. P. Loock, *Soft Matter*, 2018, **14**, 2206–2218.
17 J. E. Saunders, H. Chen, C. Brauer, M. Clayton, W. Chen, J. A. Barnes and H. P. Loock, *Soft Matter*, 2015, **11**, 8746–8757.
18 T. W. Ebbesen, H. J. Lezec, H. F. Ghaemi, T. Thio and P. A. Wolff, *Nature*, 1998, **391**, 667–669.
19 S. Nair, J. Gomez-Cruz, Á. Manjarrez-Hernandez, G. Ascanio, R. G. Sabat and C. Escobedo, *Analyst*, 2020, **145**, 2133–2142.
20 J. Gomez-Cruz, S. Nair, A. Manjarrez-Hernandez, S. Gavilanes-Parra, G. Ascanio and C. Escobedo, *Biosens. Bioelectron.*, 2018, **106**, 105–110.
21 S. G. Rodrigo, F. de Leon-Perez and L. Martin-Moreno, *Proc. IEEE*, 2016, **104**, 2288–2306.
22 X. Lan, B. Cheng, Q. Yang, J. Huang, H. Wang, Y. Ma, H. Shi and H. Xiao, *Sens. Actuators, B*, 2014, **193**, 95–99.
23 A. G. Brolo, S. C. Kwok, M. G. Moffitt, R. Gordon, J. Riordon and K. L. Kavanagh, *J. Am. Chem. Soc.*, 2005, **127**, 14936–14941.
24 C. Escobedo, *Lab Chip*, 2013, **13**, 2445–2463.
25 J. Ferreira, M. J. L. Santos, M. M. Rahman, A. G. Brolo, R. Gordon, D. Sinton and E. M. Girotto, *J. Am. Chem. Soc.*, 2008, **131**, 436–437.
26 J. Gomez-Cruz, S. Nair, G. Ascanio and C. Escobedo, SPIE Optics + Photonics Conference on Plasmonics - Design, Materials, Fabrication, Characterization, and Applications XV, San Diego, CA, 2017, SPIE-Int Soc Optical Engineering, 10346.
27 R. Gordon, D. Sinton, K. L. Kavanagh and A. G. Brolo, *Acc. Chem. Res.*, 2008, **41**, 1049–1057.
28 J. C. Yang, J. Ji, J. M. Hogle and D. N. Larson, *Biosens. Bioelectron.*, 2009, **24**, 2334–2338.

29 J. Ji, J. G. O'Connell, D. J. Carter and D. N. Larson, *Anal. Chem.*, 2008, **80**, 2491–2498.
30 L. Kalvoda, J. Jakoubková, M. Burda, P. Kwiecien, I. Richter and J. Kopecek, *Sensors*, 2023, **23**(10), 4065.
31 Y. Zhao, K. Mukherjee, K. D. Benkstein, L. Sun, K. L. Steffens, C. B. Montgomery, S. Guo, S. Semancik and M. E. Zaghloul, *Nanoscale*, 2019, **11**, 11922–11932.
32 H. Asif and R. Sahin, *Appl. Phys. B: Lasers Opt.*, 2025, **131**, 37.
33 A. González-López, J. Gomez-Cruz, G. Ascanio and C. Escobedo, *IEEE Sens. J.*, 2025, **25**, 23685–23691.
34 C. V. Rumens, M. A. Ziai, K. E. Belsey, J. C. Batchelor and S. J. Holder, *J. Mater. Chem. C*, 2015, **3**, 10091–10098.
35 P. V. Lambeck, *Meas. Sci. Technol.*, 2006, **17**, R93–R116.
36 X.-D. Wang and O. S. Wolfbeis, *Anal. Chem.*, 2016, **88**, 203–227.
37 J. Crank, *The Mathematics of Diffusion*, Oxford University Press, New York, 2nd edn, 2011.
38 R. Niemeier and J. D. Rogers, *Appl. Opt.*, 2019, **58**, 6152–6156.
39 K. Luke, Y. Okawachi, M. R. E. Lamont, A. L. Gaeta and M. Lipson, *Opt. Lett.*, 2015, **40**, 4823–4826.
40 M. N. Polyanskiy, *Sci. Data*, 2024, **11**(19), 94.
41 A. D. Rakić, A. B. Djurišić, J. M. Elazar and M. L. Majewski, *Appl. Opt.*, 1998, **37**, 5271–5283.
42 T. Thio, H. F. Ghaemi, H. J. Lezec, P. A. Wolff and T. W. Ebbesen, *J. Opt. Soc. Am. B*, 1999, **16**, 1743–1748.
43 J. Rheims, J. Köser and T. Wriedt, *Meas. Sci. Technol.*, 1997, **8**, 601–605.
44 M. Newville, R. Otten, A. Nelson, T. Stensitzki, A. Ingargiola, D. Allan, A. Fox, F. Carter and M. Rawlik, *LMFIT: Non-Linear Least-Squares Minimization and Curve-Fitting for Python*, Zenodo, bibcode: 2016ascl.soft06014N, 2016.
45 Y.-M. Sun and J. Chen, *J. Appl. Polym. Sci.*, 1994, **51**, 1797–1804.
46 K.-S. Oh, Y.-M. Koo and K.-W. Jung, *Int. J. Mass Spectrom.*, 2006, **253**, 65–70.
47 E. Boscaini, M. L. Alexander, P. Prazeller and T. D. Märk, *Int. J. Mass Spectrom.*, 2004, **239**, 179–186.